International Journal of Engineering and Geosciences
https://dergipark.org.tr/en/pub/ijeg
e-ISSN 2548-0960

3D positioning accuracy and land cover classification performance of multispectral RTK UAVs

Umut Gunes Sefercik [*1], Taskin Kavzoglu[1], Ismail Colkesen[1], Mertcan Nazar[1], Muhammed Yusuf Ozturk[1], Samed Adali [1], Salih Dinc [1]

[1]*Gebze Technical University, Faculty of Engineering, Department of Geomatics Engineering, Kocaeli, Türkiye*

Keywords
UAV
Multispectral
RTK
Machine Learning
Land Cover Classification

Research Article
DOI: 10.26833/ijeg.1074791

Received: 16.02.2022
Accepted: 19.04.2022
Published: 19.10.2022

Abstract

Lately, unmanned aerial vehicle (UAV) become a prominent technology in remote sensing studies with the advantage of high-resolution, low-cost, rapidly and periodically achievable three-dimensional (3D) data. UAV enables data capturing in different flight altitudes, imaging geometries, and viewing angles which make detailed monitoring and modelling of target objects possible. Against earlier times, UAVs have been improved by integrating real-time kinematic (RTK) positioning and multispectral (MS) imaging equipment. In this study, positioning accuracy and land cover classification potential of RTK equipped MS UAVs were evaluated by point-based geolocation accuracy analysis and pixel-based ensemble learning algorithms. In positioning accuracy evaluation, ground control points (GCPs), pre-defined by terrestrial global navigation satellite system (GNSS) measurements, were used as the reference data while Random Forest (RF) and Extreme Gradient Boosting (XGBoost) algorithms were applied for land cover classification. In addition, the spectral signatures of some major land classes, achieved by UAV MS bands, were compared with reference terrestrial spectro-radiometer measurements. The results demonstrated that the positioning accuracy of MS RTK UAV is ±1.1 cm in X, ±2.7 cm in Y, and ±5.7 cm in Z as root mean square error (RMSE). In RF and XGBoost pixel-based land cover classification, 13 independent land cover classes were detected with overall accuracies and kappa statistics of 93.14% and 93.37%, 0.92 and 0.93, respectively.

1. Introduction

In the last decades, the unmanned aerial vehicle (UAV) has become one of the most demanded remote sensing techniques due to high resolution and accurate data derived from different flight altitudes. Due to the increasing demand for high-tech equipment in various applications, the technological level of UAVs is developing day by day. For accurate orientation of the collected aerial photos without using ground control points (GCPs), UAVs have been equipped with real-time kinematic (RTK) global navigation satellite system (GNSS) receivers [1,2]. For measuring the detailed physical and chemical properties of biological materials such as agricultural products and water bodies, the multispectral and hyperspectral cameras have been integrated [3]. Besides the advantages of new technologies, some limitations still exist for the UAV technology [4,5]. No doubt, the most significant limitation is the area coverage due to low altitude legal flights. Because of that reason, a great number of flights are required for large study areas and thousands of aerial photos complicate the photogrammetric processing. In addition, the contribution levels of new technologies to the qualities of former UAV data and products are not clear in the literature.

Earth's surface and objects reflect sunlight according to their spectral reflectance characteristics.

* **Corresponding Author**

*(sefercik@gtu.edu.tr) ORCID ID 0000 – 0003 – 2403 – 5956
(kavzoglu@gtu.edu.tr) ORCID ID 0000 – 0002 – 9779 – 3443
(icolkesen@gtu.edu.tr) ORCID ID 0000 – 0001 – 9670 – 3023
(mnazar@gtu.edu.tr) ORCID ID 0000 – 0002 – 3280 – 5685
(m.ozturk2020@gtu.edu.tr) ORCID ID 0000 – 0001 – 6459 – 9356
(samed.adali2017@gtu.edu.tr) ORCID 0000 – 0002 – 6464 – 0619
(salih.dinc2017@gtu.edu.tr) ORCID 0000 – 0002 – 7641 – 8548

Cite this article

Sefercik, U. G., Kavzoglu, T., Colkesen, İ., Nazar, M., Ozturk, M. Y., Adalı, S., & Din., S. (2023). 3D positioning accuracy and land cover classification performance of multispectral RTK UAVs. International Journal of Engineering and Geosciences, 8(2), 119-128

Different technologies and methods are utilized to distinguish objects from each other by capturing and analyzing spectral reflectance. Remote sensing is a prominent technology for visualizing, processing, and interpreting spectral reflectance values. Using an image classification method on remotely sensed data, land use and land cover (LULC) of various areas can be determined. Also, thematic maps can be generated for various purposes as detection of forest areas [6], forest biomass mapping [7], farmland extraction [8], soil type detection [9], disaster monitoring and management [10-11], detection of land surface temperature [12], and monitoring of LULC change [13].

Image classification is one of the highly familiar topics in remote sensing science with decades of work on scientific literature. Moreover, establishing advanced classification techniques and improving classification accuracy is a hot topic [14-17]. Still, image classification is considered a challenging task because the classification performance can be affected by parameters such as complexity of the utilized dataset, applied image-processing method, and preferred classification technique [18]. One of the most powerful image classification approaches is machine learning which enables utilization of non-parametric and abnormal complex datasets. Also, machine learning offers higher classification accuracy against conventional algorithms in most cases [19-21]. As a concept of machine learning ensemble learning method incorporates various classifiers to generate a combined classification algorithm for increasing the robustness of the classification [22]. Furthermore, ensemble learning algorithms such as Adaptive Boosting (AdaBoost), Random Forest (RF), and Extreme Gradient Boosting (XGBoost) are commonly utilized in LULC classification studies because of their high reliability and accuracy [23,24]. In addition, apart from frequently utilized RGB imagery, multispectral, thermal and even hyperspectral sensors are used in the literature for LULC studies and research [25-29].

In this study, it is aimed to investigate the potential of RTK GNSS positioning and multispectral imaging of the UAVs. Accordingly, the data derived from DJI Phantom IV Multispectral RTK, one of the most preferred UAVs for particularly agricultural purposes, was comprehensively investigated. The geolocation accuracy of the UAV was analyzed by comparing the results of image orientation with and without GCPs. The performances of the UAV's spectral bands were analyzed by comparing spectral reflectance values derived from reference spectro-radiometer measurements on the ground [30]. Moreover, the land cover classification potential of the multispectral UAV was analyzed with RF and XGBoost pixel-based classification algorithms using 13 independent land cover classes [31-33].

2. Study Area and Materials

2.1. Study Area

The study area is a part of Gebze Technical University (GTU) Campus located in Kocaeli Metropolitan, Turkey. The size of the area is 500 m×225 m covering several land classes such as cultivated areas, different species of trees, meadow, soil and buildings. The topography is mostly flat and orthometric heights are between 4 m and 20 m. Figure 1 shows the location and orthomosaic of the study area and an instance aerial photo in NIR (near-infrared) imaging band. Figure coordinates are geographical, and the datum is WGS84 (World Geodetic System 1984).

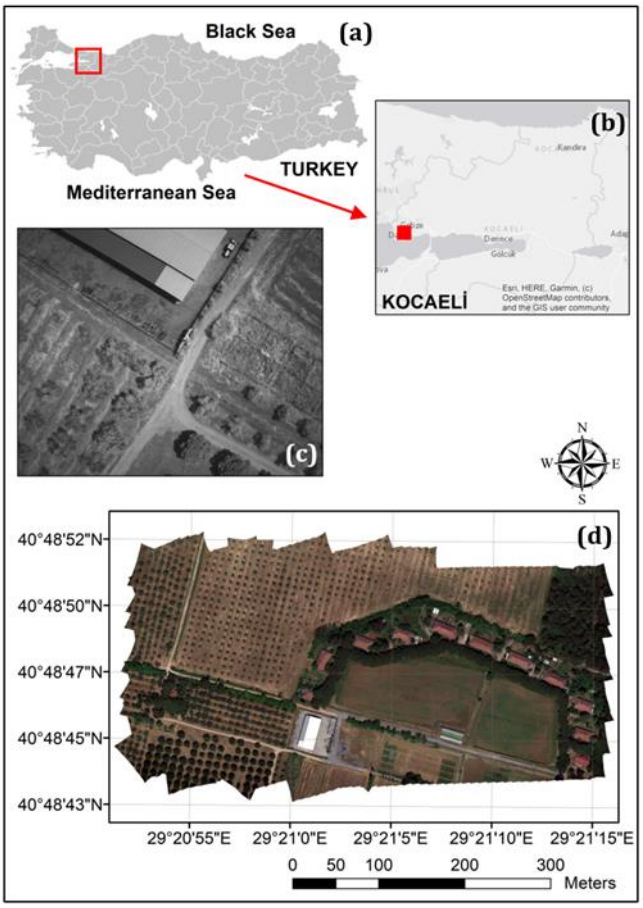

Figure 1. Location of the Kocaeli Metropolitan in Turkey (a), location of the GTU Campus in Kocaeli (b), an instance of NIR band aerial photo (c) and UAV orthomosaic of the study area (d)

2.2. Materials

In the study, UAV flights were completed with DJI Phantom IV Multispectral RTK UAV with six imaging bands as RGB, red, green, blue, red edge (RE) and NIR. For the spectral reflectance calibration, MAPIR Camera Reflectance Calibration Ground Target Package V2 which has four different targets in different colors as black, dark gray, light gray and white was utilized. Reference GCP surveys and spectral measurements in the field were completed by using CHC i80 GNSS receiver and ASD Fieldspec3 spectro-radiometer, respectively. Figure 2 illustrates the utilized UAV and reflectance calibration target. The properties of the utilized UAV are presented in Table 1. The diffuse reflectance values used in spectral reflectance calibration of aerial photos and reflectance curves are displayed in Table 2 and Figure 3. The total of used materials is available at GTU Geomatics Engineering Department's Advanced Remote Sensing Technology Laboratory (ARTLAB).

Table 1. Properties of DJI Phantom IV Multispectral UAV

Property	Value
Camera	Six 1/2.9" CMOS sensors including one RGB and five monochromes with effective pixel resolution of 2.08 megapixel
Sensor wavelengths	Blue (B): 450 nm ± 16 nm; Green (G): 560 nm ± 16 nm; Red (R): 650 nm ± 16 nm; Red edge (RE): 730 nm ± 16 nm; Near-infrared (NIR): 840 nm ± 26 nm
Gimbal	3-axis as pitch, roll, yaw
Flight duration	Approx. 27 minutes
Weight	1487 g
Speed	14 m/s in P-mod; 16 m/s in A-mod
Wind speed resistance	Max. 10 m/s
Operating temperature	0° to 40°C
Outdoor positioning module	GPS, GLONASS, Galileo, Beidou
Hover accuracy range	RTK enabled: ± 0.1 m V, ± 0.1 m H; RTK disabled: ± 0.1 m V, ± 0.3 m H (Vision); ± 0.5 m V, ± 1.5 m H (GPS)
Positioning accuracy RTK	1 cm + 1 ppm Horizontal; 1.5 cm + 1 ppm Vertical

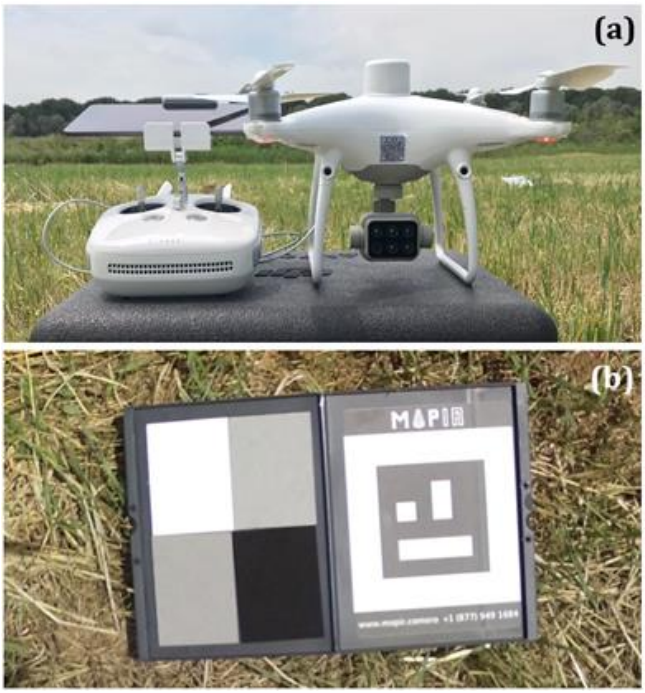

Figure 2. Utilized DJI Phantom IV Multispectral UAV (a) and MAPIR Camera Reflectance Calibration Ground Target Package V2 (b)

Table 2. Reference diffuse reflectance values for MAPIR camera calibration ground target

	Camera Calibration Ground Targets			
Bands	Black	Dark Gray	Light Gray	White
Blue	0.020136	0.182556	0.247980	0.791917
Green	0.019630	0.193762	0.263037	0.866432
Red	0.019371	0.198543	0.262901	0.871958
RE	0.019563	0.212881	0.262741	0.869990
NIR	0.021459	0.228368	0.275486	0.862524

3. Methodology

The used methodology has five different stages as UAV data acquisition and reference terrestrial surveys, image alignment and dense cloud generation, reflectance calibration and orthomosaic generation, pixel-based land cover classification, and accuracy validations. UAV data processing steps were accomplished utilizing Agisoft Metashape Professional, a structure from motion (SfM) based image matching software. Land cover classification using RF and XGBoost pixel-based classification algorithms were achieved in the RStudio which operates based on the R programming language. In Figure 4, conducted methods are shown with utilized software packages.

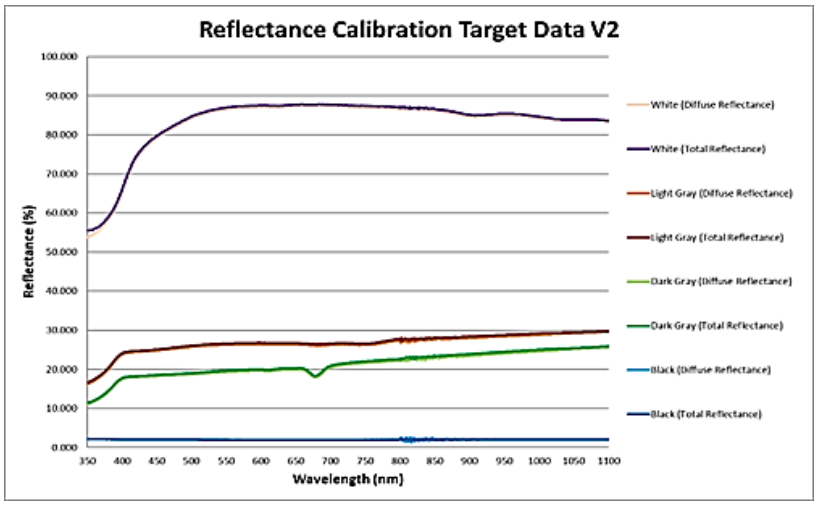

Figure 3. Reflectance curve graph of the MAPIR reflectance calibration targets

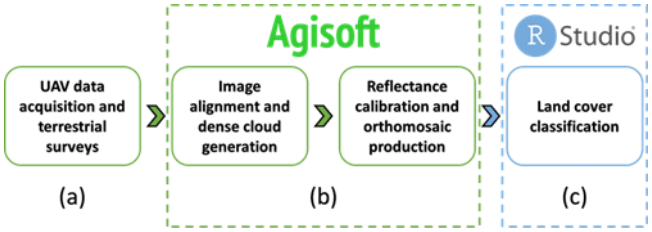

Figure 4. Methods of the study including UAV data acquisition and terrestrial surveys (a), UAV data processing in Agisoft Metashape (b) and land cover classification using RStudio (c)

3.1. UAV data acquisition and terrestrial surveys

UAV data acquisition was carried out by preparing UAV flight plans using DJI GS (Ground Station) PRO UAV flight planning software. In the utilized software two UAV flights were designed considering coarse strip angles in polygonal mode to cover whole study area with the minimum number of photos (Figure 5).

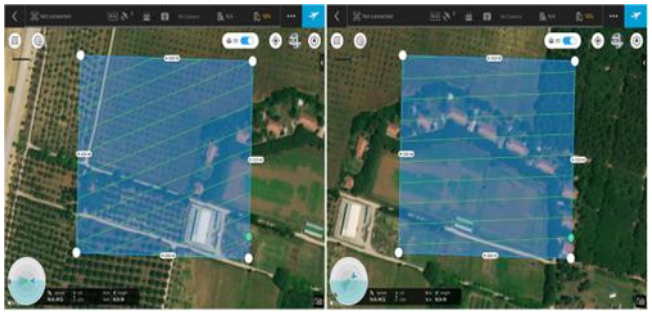

Figure 5. UAV flight plans showing the first (left) and second (right) polygonal flights

For more realistic surface determination of terrain and non-terrain objects, ground sampling distance (GSD), definition of spatial resolution, is one of the most significant parameters. In UAV flights, GSD is directly proportional with flight altitude and minimum GSD can be obtained with minimum flight altitude according to the following equation (1). Here, an important note: lower altitude means more aerial photos to stereo coverage of the study area. That's why, number of required photos should be considered when adjusting the flight altitude and GSD.

$$\frac{f}{h} = \frac{p}{GSD} \quad (1)$$

Where, f is the focal length of used digital camera, p is the pixel size of camera sensor and h is the flight altitude. During the polygonal UAV flights, the flying altitude was selected as 70 m considering the highest objects in flight plans, number of aerial photos for fully stereo coverage and high spatial resolution (3.66 cm GSD). In addition, the minimum overlap ratios for front and side were preferred as 80% and %60, respectively to increase the quality of stereo matching, depth extraction and generated digital surface model (DSM) used for true orthomosaic production. Image capture time interval and UAV flight speed were set to two seconds and 5 m/s, respectively. With UAV flights, 530 aerial photos were obtained. Before the flights, IMU (Inertial Measurement Unit), compass, gimbal and vision sensors of the UAV were calibrated and the photos of the MAPIR reflectance panel were taken. Moreover, in-situ spectro-radiometer surveys were conducted simultaneously with UAV flights to measure reflectance values in the same lighting conditions with captured aerial photos. Reflectance values obtained from the in-situ spectro-radiometer measurements for blue, green, red, RE and NIR bands were used to validate pixel-based land cover classification results.

In normal conditions, RTK GNSS equipped DJI Phantom IV Multispectral does not require GCPs for image orientation. However, for point-based geolocation accuracy analysis, nine independent GCPs were established in the area and measured by utilizing Continuously Operating Reference Stations (CORS) RTK GNSS method. Figure 6 shows the distribution of established GCPs over the study area, an instance terrestrial GCP measurement and a photo captured by the UAV on the ground for reflectance calibration.

When capturing a proper photo by UAV camera for reflectance calibration, some requirements should be considered. First, the calibration panel should be placed in a flat terrain, fully and centrally displayed on the UAV image and not be obstructed by any shadow or material. Second, the image of the calibration panel should be captured from a maximum height depending on the manufacturer recommendation. For MAPIR reflectance calibration panel, utilized in this study, the maximum height for image capturing was declared as 15 feet (~4.5 m) [34]. For better determination of the MAPIR calibration panel with higher spatial resolution and more accurate masking process, we recommend ~1.5 m distance between UAV camera and the calibration panel for best calibration performance.

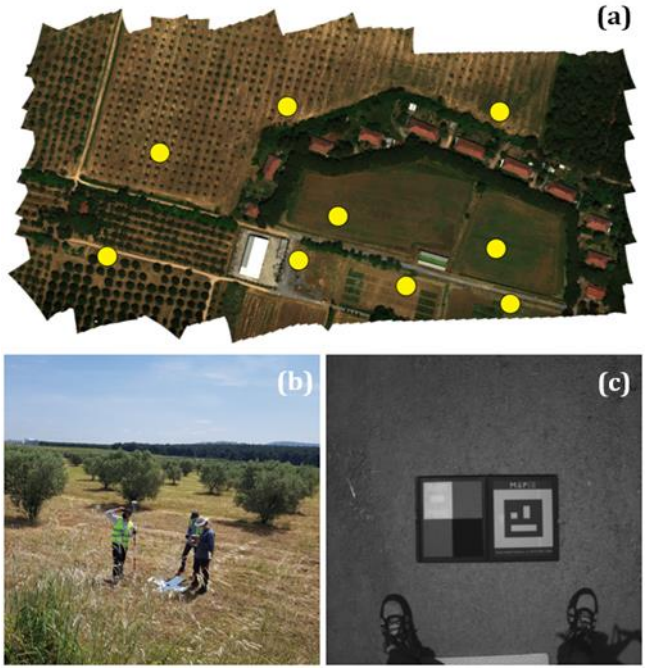

Figure 6. GCP distribution over the study area (a), an instance terrestrial GCP measurement (b) and an instance photo taken for reflectance calibration (c)

3.2. Image alignment and dense cloud generation

Image alignment procedure was done in Agisoft Metashape, a SfM based photogrammetric image matching software. The SfM algorithm operates based on the stereoscopic viewing principle to extract and build 3D geometry utilizing a set of overlapping photos with an offset (base) value [36-41]. In other words, using the SfM technique, photos of an object from multiple viewpoints are taken to realize camera positions and orientations for establishing a spatial connection between common points. Image alignment was performed using aerial photos, yielding a sparse point cloud containing approx. 3 million points. Because of the precise coordinates of the UAV data, the geometric correction was carried out without the GCPs, resulting in a shorter and more efficient alignment process. After the alignment process, a dense point cloud of approx. 38 million points was obtained by extracting depth maps from aerial photos. To eliminate the noise effects especially in the areas with dense trees, dense point clouds were filtered by fencing and classifying noisy points (Figure 7). Generated sparse and dense point clouds are represented in Figure 8.

3.3. Reflectance calibration and orthomosaic production

Obtaining the appropriate spectral data from the imagery is an essential task in land cover classification. Therefore, it is of utmost importance to capture the reflectance values of objects to make accurate analyses. It is required to calibrate the imagery, obtained using different imaging bands, using a sensor calibration method such as a ground reflectance target. Ground reflectance targets are measured in an ideally illuminated environment to acquire reference spectral values. Utilizing reference spectral reflectance data, aerial photos can be calibrated. Therefore, using calibration photos with reference diffuse reflectance values and sun sensor data from the UAV, the camera reflectance calibration process was realized. During the calibration process, all of the calibration targets were masked individually to isolate the target from the rest for an accurate operation (Figure 9) [42].

Using the dense point cloud data, a 7 cm gridded DSM was generated for utilizing in true-orthomosaic production. Finally, a 16-bit orthomosaic with a pixel resolution of 3.66 cm (same as the GSD) was produced using both calibrated aerial photos and the DSM.

3.4. Land cover classification

Before the land cover classification, 13 land cover classes were determined as concrete, coniferous, cultivated, deciduous, meadow, non-cultivated, olive trees, pasture, shadow, soil, tile-roof, water, white roof in the study area. Utilizing the RStudio, an open-source software for data science, pixel-based ensemble learning classification approaches RF and XGBoost were used to classify the calibrated UAV orthomosaic. To test the performance of multispectral UAV data in land cover classification, RE and NIR bands were utilized to calculate some vegetation indices (VIs) as Normalized Difference Vegetation Index (NDVI) and the Normalized Difference Red Edge Index (NDRE). Moreover, NDVI and NDRE data were appended to calibrated orthomosaic with 5-bands (red, green, blue, RE, NIR) as the 6th and 7th bands, respectively, by layer stacking process. A sufficient number of test and training data were collected for each land cover class during the sample gathering process. Table 3 shows the total training and test pixel counts.

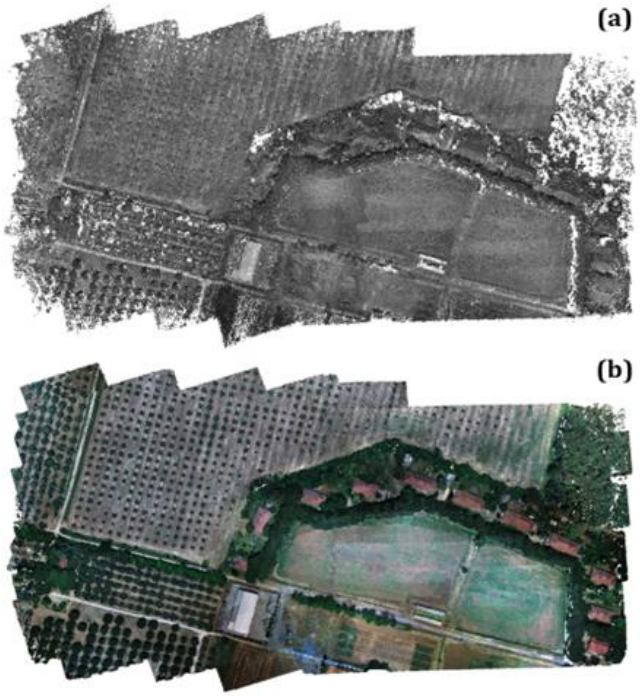

Figure 7. Generated sparse (a) and dense point clouds (b)

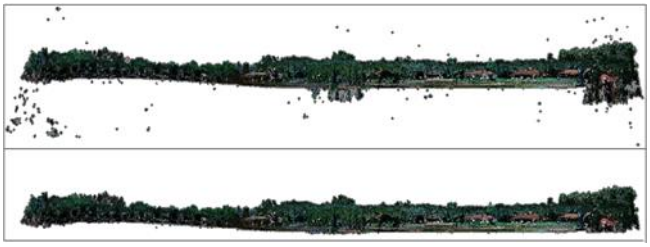

Figure 8. Noisy (upper) and filtered (lower) dense point clouds

Table 3. Total training and test pixel counts in each class

Land Cover Class	Total Training Pixel	Total Test Pixel
Concrete	5547	15139
Coniferous	5102	15524
Cultivated	5128	15417
Deciduous	5176	15325
Meadow	5270	15173
Non-cultivated	5230	15280
Olive trees	5088	15229
Pasture	5390	15649
Shadow	5034	15088
Soil	5098	15169
Tile-roof	5135	15003
Water	5298	15724
White-roof	5259	15304

4. Results and Discussion

Figure 10 shows the spectral signatures of independent land cover classes detected by in-situ spectro-radiometer measurements.

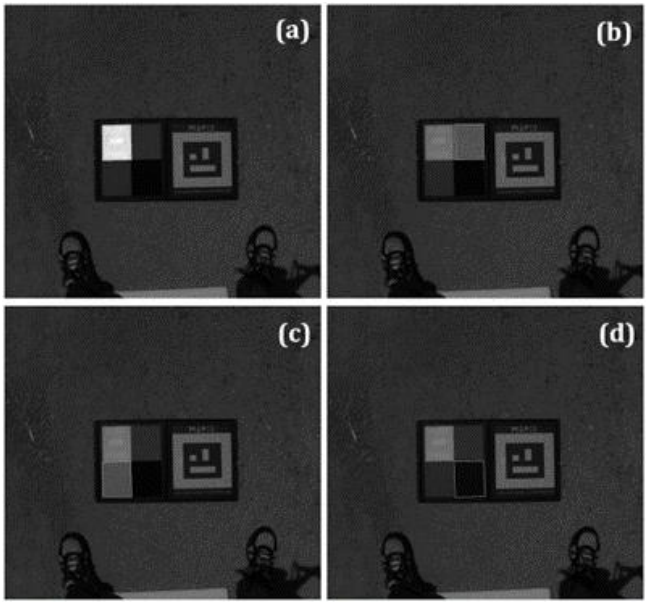

Figure 9. Masked reflectance targets: (a) white, (b) light gray, (c) dark gray and (d) black

Table 4 presents the GCP-based positioning accuracy results of multispectral RTK UAV. In accuracy validation, the reference GCPs, measured by terrestrial GNSS measurements, were found on the generated UAV orthomosaic and the X, Y, Z values were compared. The results demonstrated that RTK UAV positioning accuracy is ±1.1 cm in X, ±2.7 cm in Y, and ±5.7 cm in Z as RMSE. With the highest RMSE value (± 5.7 cm) in Z-direction, it is observed that the performance of UAV RTK GNSS is lower in vertical positioning in comparison with horizontal.

Figure 11 displays the generated orthomosaic before and after spectral reflectance calibration process. The great importance of spectral calibration is clear in the Figure. Without spectral reflectance calibration the land cover classification results will be misleading.

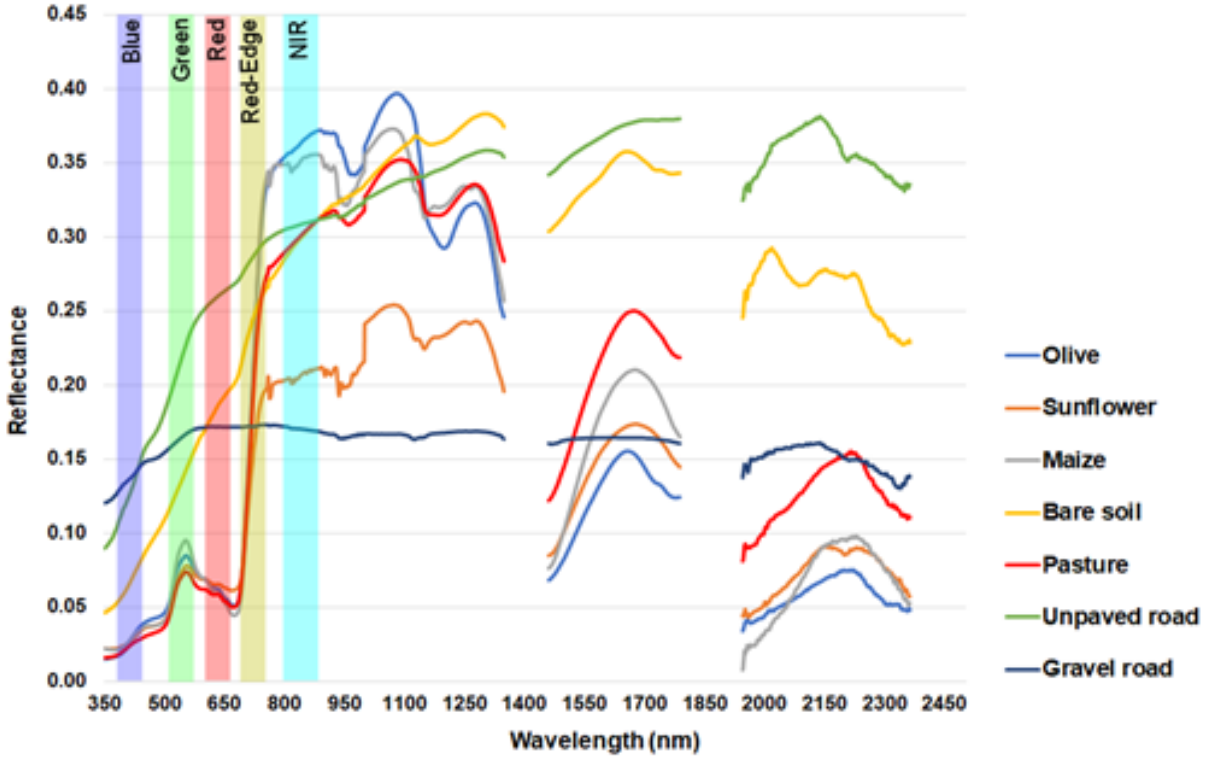

Figure 10. Spectral signatures of land cover classes determined by in-situ spectro-radiometer measurements

Table 4. 3D geolocation accuracy point-based evaluation results obtained by comparing terrestrial GNSS measurements with GCP coordinates acquired from orthomosaic

GCP	Terrestrial Measurements			UAV RTK GNSS			Errors (±)		
	X (m)	Y (m)	Z (m)	X (m)	Y (m)	Z (m)	ΔX (m)	ΔY (m)	ΔZ (m)
1	445408.933	4520098.918	51.970	445408.944	4520098.875	51.903	0.011	0.043	0.067
2	445322.326	4519934.340	46.441	445322.331	4519934.339	46.447	0.005	0.001	0.006
3	445419.067	4519917.866	45.603	445419.074	4519917.866	45.646	0.007	0.000	0.043
4	445044.946	4519962.328	53.575	445044.934	4519962.314	53.550	0.012	0.014	0.025
5	445212.315	4520103.774	52.226	445212.326	4520103.725	52.179	0.011	0.049	0.047
6	445259.375	4520000.639	48.369	445259.385	4520000.629	48.439	0.010	0.010	0.070
7	445406.205	4519969.530	47.736	445406.228	4519969.528	47.800	0.023	0.002	0.064
8	445094.118	4520060.561	54.458	445094.124	4520060.516	54.356	0.006	0.045	0.102
9	445222.708	4519959.093	47.992	445222.710	4519959.089	48.013	0.002	0.004	0.021

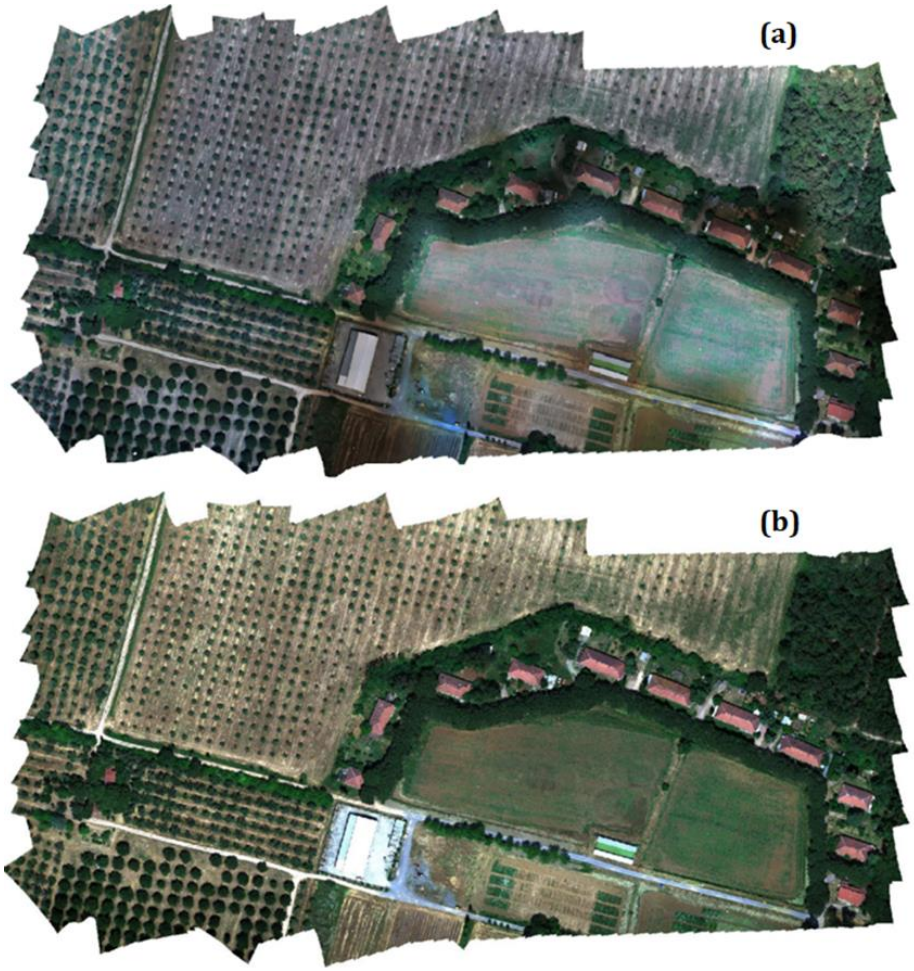

Figure 11. Non-calibrated orthomosaic (a) and calibrated orthomosaic (b) of the study area

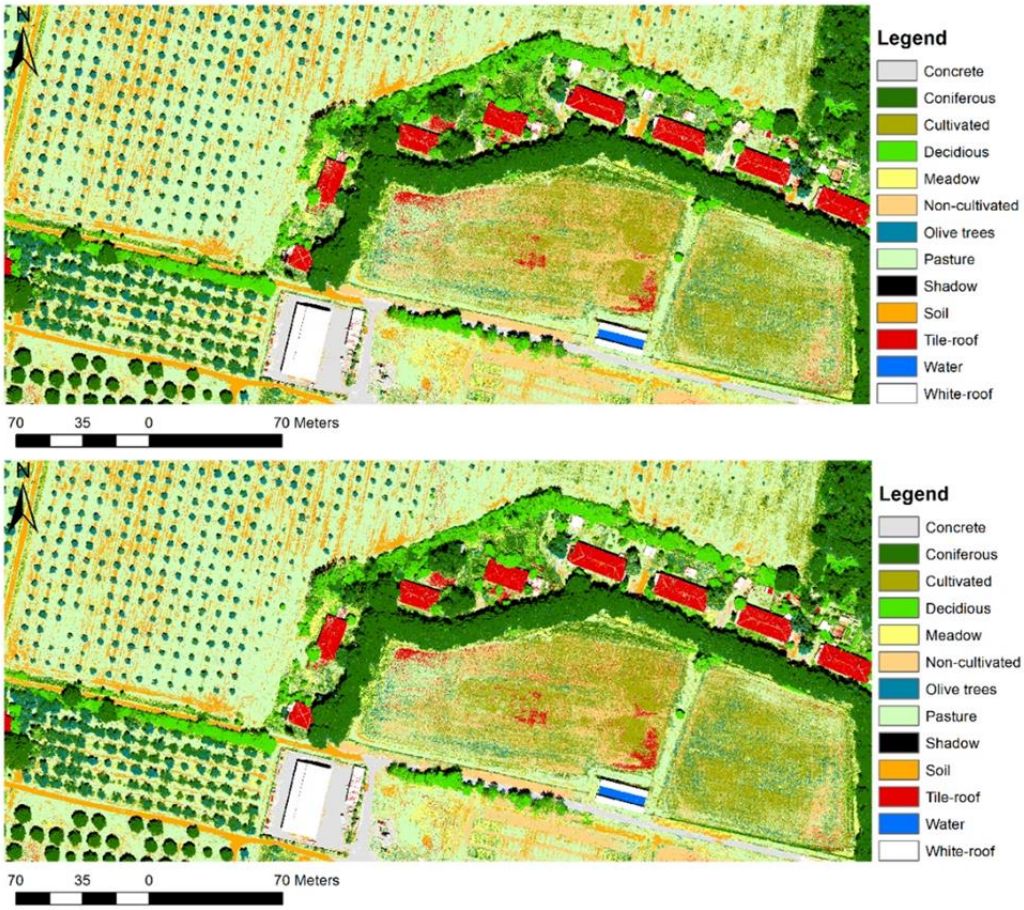

Figure 12. RF (upper) and XGBoost (lower) pixel-based classification results, orthomosaic cropped for the convenience

Classification maps of the RF and XGboost ensemble learning pixel-based classifiers are given in Figure 12. Classification results were checked by overall accuracy, kappa and F-score statistics for the purpose of evaluating the land cover classification performance of the utilized MS UAV (Table 5). Also, a confusion matrix was prepared to interpret the classification results in detail providing further insight about the land cover classes (Table 6).

The results demonstrated that both classifiers have high performance and have very similar results for each land cover class. While the XGBoost algorithm slightly outperformed the RF by overall accuracy, the difference is relatively small. Both classifiers have overall accuracies of more than 93% and kappa statics of greater than 0.9. Also, for RF and XGBoost classification methods minimum and maximum F-scores are relatively close, 82.89% and 84.19%, 99.97% and 99.92%, respectively. The lowest accuracies exist in meadow, cultivated and deciduous land cover classes. The complex and dynamic structure of the densely forested or vegetated areas can have an influence on classification results. In addition, due to being very sensitive to changes in the environment as the season of the year, wind and lighting conditions, regions with trees or different vegetation covers can have differentiating spectral signatures.

Table 5. RF and XGBoost pixel-based classification results showing F-scores of each land cover class, overall accuracy, and kappa statistic

Measurement	Land Cover Class	RF	XGBoost
	Concrete	98.21	98.28
	Coniferous	85.03	85.37
	Cultivated	88.72	88.90
	Deciduous	89.03	88.89
	Meadow	82.89	84.19
	Non-cultivated	93.99	94.63
F-score	Olive trees	91.66	92.52
	Pasture	94.36	94.65
	Shadow	97.58	97.48
	Soil	98.52	98.27
	Tile-roof	97.12	96.86
	Water	99.97	99.92
	White-roof	93.66	93.96
Overall accuracy	Whole area	93.14	93.37
Kappa	Whole area	0.92	0.93

Table 6. Confusion matrix results of the RF and XGBoost classification algorithms

RF Classification

	A	B	C	D	E	F	G	H	I	J	K	L	M	UA
A	14799	0	0	0	0	5	0	0	0	9	0	0	151	98.95
B	0	13723	232	710	572	0	667	4	703	0	14	0	0	82.00
C	0	1132	14444	716	320	1	423	75	0	0	0	0	3	84.50
D	0	109	29	13366	1306	0	1	0	0	0	0	0	0	89.64
E	0	405	91	396	12049	0	481	28	0	0	0	0	0	89.02
F	0	0	8	0	0	14209	0	120	0	0	120	0	295	95.80
G	0	118	122	73	320	0	13647	1	0	0	0	0	2	94.97
H	1	2	400	0	569	229	0	15277	0	95	41	0	11	91.70
I	0	37	0	2	0	0	0	0	14383	0	0	0	0	99.63
J	11	0	0	0	28	4	0	52	0	15006	257	0	0	98.08
K	0	0	54	0	9	28	0	99	2	71	14522	0	199	97.18
L	0	0	0	0	0	0	0	0	0	0	0	15698	0	100.00
M	340	0	2	0	0	804	0	0	0	0	49	26	14643	91.53
PA	97.49	88.29	93.39	88.44	77.55	92.24	88.58	97.18	95.61	98.97	97.05	99.94	95.88	

XGBoost Classification

	A	B	C	D	E	F	G	H	I	J	K	L	M	UA
A	14771	0	0	0	0	3	0	0	0	3	0	0	151	98.90
B	0	13708	256	695	684	0	712	4	658	0	1	0	0	82.54
C	0	1118	14365	617	363	1	462	73	0	0	0	0	1	84.40
D	0	146	38	13498	1374	0	2	0	0	0	0	0	0	90.24
E	0	382	109	356	11767	0	561	35	0	8	0	0	0	89.58
F	2	0	39	0	0	14095	0	141	0	0	131	0	305	96.32
G	0	128	159	86	340	0	13481	1	0	0	0	0	0	95.55
H	0	2	381	0	624	235	1	15215	0	69	58	0	8	91.89
I	0	42	0	11	0	0	0	0	14426	0	0	0	0	99.73
J	15	0	0	0	21	6	0	54	0	15025	198	0	0	97.71
K	0	0	28	0	0	16	0	133	4	76	14561	0	166	96.92
L	0	0	0	0	0	0	0	0	0	0	0	15715	0	100.00
M	363	0	7	0	0	924	0	0	0	0	54	9	14673	92.30
PA	97.68	88.39	93.90	87.57	79.41	92.99	89.67	97.58	95.33	98.85	96.79	99.83	95.68	

Note: Class keys are A: Concrete; B: Coniferous; C: Cultivated; D: Deciduous; E: Meadow; F: Non-cultivated; G: Olive trees; H: Pasture; I: Shadow; J: Soil; K: Tile-roof; L: Water; M: White-roof. UA: User's accuracy; PA: Producer's accuracy.

5. Conclusion

In the study, the 3D positioning accuracy and land cover classification performance of one of the most common MS RTK equipped UAVs DJI Phantom IV MS was investigated. The results demonstrated that the positioning accuracy of the device is ±1.1 cm in X, ±2.7 cm in Y and ±5.7 cm in height as RMSE. The positioning accuracy is higher in planimetric directions in comparison with vertical direction. In land cover classification side, the overall accuracies are more than 93% both for RF and XGBoost pixel-based ensemble learning classifiers. The kappa statistics are 0.92 and 0.93 and F-scores of independent land cover classes fluctuate

between 82.89% - 99.97% and 84.19% - 99.92% for RF and XGBoost, respectively. While looking at F-scores of each land cover class, the lowest accuracies were obtained in forest and vegetated areas.

Acknowledgement

We would like to thank TÜBİTAK for supporting this study within the scope of 2209-A University Students Research Projects Support Program.

Author contributions

Umut Gunes Sefercik: Planning, aerial data acquisition and processing, terrestrial measurements, analysis, validation, paper preparation. **Taskin Kavzoglu:** Planning, validation, paper preparation. **Ismail Colkesen**: Planning, terrestrial measurements, analysis, validation, paper preparation. **Mertcan Nazar:** Aerial data acquisition and processing, terrestrial measurements, analysis, validation, paper preparation. **Muhammed Yusuf Ozturk:** Terrestrial measurements, analysis. **Samed Adali:** Aerial data acquisition and processing, terrestrial measurements, analysis. **Salih Dinc:** Aerial data acquisition and processing, terrestrial measurements, analysis.

Conflicts of interest

The authors declare no conflicts of interest.

References

1. Rabah, M., Basiouny, M., Ghanem, E., & Elhadary, A. (2018). Using RTK and VRS in direct geo-referencing of the UAV imagery. NRIAG Journal of Astronomy and Geophysics. 7(2), 1-7.
2. Ekaso, D., Nex, F., & Kerle, N. (2020). Accuracy assessment of real-time kinematics (RTK) measurements on unmanned aerial vehicles (UAV) for direct geo-referencing, Geo-spatial Information Science, 23(2), 165-181.
3. Bae, J., Bae, H., Kim, G., Park, E., & Cho, B. (2020). Development of unmanned aerial vehicle remote sensing technology for abiotic stress monitoring of citrus 'Unshiu' using multispectral imaging. Journal of the Korean Society for Nondestructive Testing, 40, 274-284.
4. Fields, N. R. (2012). Advantages and challenges of unmanned aerial vehicle autonomy in the Postheroic age. Master's Thesis, James Madison University, 205.
5. Forsman, J., & Westergren, M. (2019). Potential and limitations with UAV deliveries to ships at sea, Bachelor's Thesis in Marine Engineering, Department of Mechanics and Maritime Sciences, Chalmers University of Technology, 1-38.
6. Fraser, B. T., & Congalton, R. G. (2019). Evaluating the effectiveness of Unmanned Aerial Systems (UAS) for collecting thematic map accuracy assessment reference data in New England forests. Forests, 10(1), 24.
7. Du, L., Zhou, T., Zou, Z., Zhao, X., Huang, K., & Wu, H. (2014). Mapping forest biomass using remote sensing and national forest inventory in China. Forests, 5(6), 1267-1283.
8. Sun, Z., Wang, D., & Zhong, G. (2018). Extraction of farmland geographic information using OpenStreetMap data. In 2018 7th International Conference on Agro-geoinformatics, 1-4.
9. Kempen, B., Brus, D. J., & Heuvelink, G. B. (2012). Soil type mapping using the generalised linear geostatistical model: A case study in a Dutch cultivated peatland. Geoderma, 189, 540-553.
10. Kavzoglu, T., Teke, A., & Yilmaz, E. O. (2021). Shared blocks-based ensemble deep learning for shallow landslide susceptibility mapping. Remote Sensing, 13(23), 4776.
11. Rahaman, S. M., Khatun, M., Garai, S., Das, P., & Tiwari, S. (2022). Forest Fire Risk Zone Mapping in Tropical Forests of Saranda, Jharkhand, Using FAHP Technique. In Geospatial Technology for Environmental Hazards, 177-195, Springer, Cham.
12. Şekertekin, A., & Marangoz, A. M. (2019). Zonguldak metropolitan alanındaki arazi kullanımı arazi örtüsünün yer yüzey sıcaklığına etkisi. Geomatik, 4(2), 101-111.
13. Yılmaz, O. S., Gülgen, F., Güngör, R., & Kadı, F. (2018). Uzaktan algılama teknikleri ile arazi kullanım değişiminin incelenmesi: Köprübaşı İlçesi örneği. Geomatik, 10, 233-241.
14. Harsanyi, J. C., & Chang, C. I. (1994). Hyperspectral image classification and dimensionality reduction: An orthogonal subspace projection approach. IEEE Transactions on Geoscience and Remote Sensing, 32(4), 779-785.
15. Chapelle, O., Haffner, P., & Vapnik, V. N. (1999). Support vector machines for histogram-based image classification. IEEE Transactions on Neural Networks, 10(5), 1055-1064.
16. Ciregan, D., Meier, U., & Schmidhuber, J. (2012). Multi-column deep neural networks for image classification. IEEE Conference on Computer Vision and Pattern Recognition, 3642-3649.
17. Lavreniuk, M., Kussul, N., & Novikov, A. (2018). Deep learning crop classification approach based on sparse coding of time series of satellite data. In IEEE International Geoscience and Remote Sensing Symposium, 4812-4815.
18. Lu, D., & Weng, Q. (2007). A survey of image classification methods and techniques for improving classification performance. International Journal of Remote Sensing, 28(5), 823-870.
19. Hansen, M., Dubayah, R., & DeFries, R. (1996). Classification trees: an alternative to traditional land cover classifiers. International Journal of Remote Sensing, 17(5), 1075-1081.
20. Rogan, J., Miller, J., Stow, D., Franklin, J., Levien, L., & Fischer, C. (2003). Land-cover change monitoring with classification trees using Landsat TM and ancillary data. Photogrammetric Engineering & Remote Sensing, 69(7), 793-804.
21. Mondal, A., Kundu, S., Chandniha, S. K., Shukla, R., & Mishra, P. K. (2012). Comparison of support vector machine and maximum likelihood classification technique using satellite imagery. International Journal of Remote Sensing and GIS, 1(2), 116-123.

22. Pal, M. (2008). Ensemble of support vector machines for land cover classification. International Journal of Remote Sensing, 29(10), 3043-3049.
23. Chan, J. C. W., & Paelinckx, D. (2008). Evaluation of Random Forest and Adaboost tree-based ensemble classification and spectral band selection for ecotope mapping using airborne hyperspectral imagery. Remote Sensing of Environment, 112(6), 2999-3011.
24. Georganos, S., Grippa, T., Vanhuysse, S., Lennert, M., Shimoni, M., & Wolff, E. (2018). Very high resolution object-based land use–land cover urban classification using extreme gradient boosting. IEEE Geoscience and Remote Sensing Letters, 15(4), 607-611.
25. Sun, L., & Schulz, K. (2015). The improvement of land cover classification by thermal remote sensing. Remote sensing, 7(7), 8368-8390.
26. Sefercik, U. G., Kavzoglu, T., Colkesen, I., Adali, S., Dinc, S., Nazar, M., & Ozturk, M. Y. (2021). Land cover classification performance of multispectral RTK UAVs. The International Archives of Photogrammetry, Remote Sensing and Spatial Information Sciences, XLVI-4-W5-2021, 489-492.
27. Bhosle, K., & Musande, V. (2019). Evaluation of deep learning CNN model for land use land cover classification and crop identification using hyperspectral remote sensing images. Journal of the Indian Society of Remote Sensing, 47(11), 1949-1958.
28. Avcı, C., Budak, M., Yağmur, N. & Balçık, F. (2023). Comparison between random forest and support vector machine algorithms for LULC classification. International Journal of Engineering and Geosciences, 8 (1), 1-10. https://doi.org/10.26833/ijeg.987605
29. Khorrami, B., Gunduz, O., Patel, N., Ghouzlane, S., & Najjar, M. (2019). Land surface temperature anomalies in response to changes in forest cover. International Journal of Engineering and Geosciences, 4(3), 149-156.
30. Jenal, A., Lussem, U., Bolten, A., Gnyp, M., Schellberg, J., Jasper, J., Bongartz, J., & Bareth, G. (2020). Investigating the potential of a newly developed UAV-based VNIR/SWIR imaging system for forage mass monitoring. PFG – Journal of Photogrammetry Remote Sensing and Geoinformation Science, 88, 493-507.
31. Chen, T., & Guestrin, C. (2016). XGBoost: A scalable tree boosting system. In Proceedings of the 22nd ACM SIGKDD International Conference on Knowledge Discovery and Data Mining; Association for Computing Machinery, San Francisco, CA, USA, 785-794.
32. Ma., L., Zhou, M., & Li, C. (2017). Land covers classification based on Random Forest method using features from full-waveform lidar data, International Archives of the Photogrammetry, Remote Sensing and Spatial Information Sciences, 42(2/W7), 263-268.
33. Zhang, W., Li, W., Zhang, C., Hanink, D. M., Li, X., & Wang, W. (2017). Parcel-based urban land use classification in megacity using airborne LiDAR, high resolution orthoimagery, and Google Street View. Computer Environment Urban Systems, 64, 215-228.
34. MAPIR calibration target capture procedure, https://www.mapir.camera/pages/calibration-target-capture-procedure-v2
35. Westoby, M. J., Brasington, J., Glasser, N. F., Hambrey, M. J., & Reynolds, J. M. (2012). 'Structure-from-Motion'photogrammetry: A low-cost, effective tool for geoscience applications. Geomorphology, 179, 300-314.
36. Sefercik, U. G., Tanrikulu, F., & Atalay, C. (2019). Photogrammetric 3D modelling potential comparison of SFM-based new generation image matching software. In The 40th Asian Conference on Remote Sensing, Korea.
37. Yakar, M., & Dogan, Y. (2018, November). 3D Reconstruction of Residential Areas with SfM Photogrammetry. In Conference of the Arabian Journal of Geosciences (pp. 73-75). Springer, Cham.
38. Şasi, A. & Yakar, M. (2018). Photogrammetric modelling of Hasbey Dar'ülhuffaz (Masjid) using an unmanned aerial vehicle. International Journal of Engineering and Geosciences, 3 (1), 6-11.
39. Yakar, M., & Doğan, Y. (2018). GIS and three-dimensional modeling for cultural heritages. *International Journal of Engineering and Geosciences*, *3*(2), 50-55.
40. Ulvi, A., Yakar, M., Yiğit, A. Y. & Kaya, Y. (2020). İha Ve Yersel Fotogrametrik Teknikler Kullanarak Aksaray Kızıl Kilisenin 3b Modelinin Ve Nokta Bulutunun Elde Edilmesi. Geomatik, 5 (1), 19-26.
41. Mırdan, O. & Yakar, M. (2017). Tarihi Eserlerin İnsansız Hava Aracı İle Modellenmesinde Karşılaşılan Sorunlar. Geomatik, 2 (3), 118-125.
42. Teixeira, A. A., Mendes Júnior, C. W., Bredemeier, C., Negreiros, M., Aquino, R. D. S. (2020). Evaluation of the radiometric accuracy of images obtained by a Sequoia multispectral camera. Engenharia Agrícola, 40, 759-768.